

Achieving High Aqueous Energy Storage via Hydrogen-Generation Passivation

Yuhang Wang, Xiaoqi Cui, Yueyu Zhang, Lijuan Zhang, Xingao Gong,*
and Gengfeng Zheng*

Aqueous rechargeable lithium-ion batteries (ARLIBs) represent an extremely attractive candidate for next-generation energy-storage devices, attributed to their excellent theoretical power density, high ionic conductivity, nonflammability, and low cost.^[1–3] Nonetheless, compared to their nonaqueous counterparts, the development of ARLIBs has been critically limited by their much narrower electrochemical potential windows (typically <1.8 V) and lower energy densities,^[4,5] which are predominantly restrained by ubiquitous side reactions in aqueous solutions, i.e., electrochemical water splitting.^[6] Although the sluggish oxygen evolution usually requires a large overpotential, the hydrogen-evolution reaction (HER) can easily take place when the applied potential increases, and thereby serves as a critical constraining factor for the battery voltage working window as well as the output Coulombic efficiency.^[2,6] Although using alkaline electrolytes can shift the water reduction potential and allow for the functionality of anode materials,^[1,7] the water oxidation potential also shifts downward, and thus the existence of water splitting with a thermodynamic potential of 1.23 V still results in a significant loss of Coulombic efficiency.^[7] It was recently reported that using highly concentrated (molality > 20 m) organic Li⁺ salt-based aqueous electrolytes can expand the voltage window.^[8] However, such high salt concentrations inevitably lead to a much slower reaction kinetics of ARLIBs, and thereby a limited high-power feature.

The rational design of anode materials, in which the water reduction also takes place, may suggest a new avenue for ARLIB discovery with enhanced voltage window and power density. Our design was inspired by the recent research hotspots of developing new hydrogen-evolution catalysts that can reduce the overpotentials of hydrogen formation.^[9–11] The opposite strategy instead, aiming to create a large HER overpotential for inhibiting water reduction and subsequently enhancing both the battery output potential and Coulombic efficiency in

aqueous solutions, has never been demonstrated. Moreover, an electrode surface passivated with hydrogen evolution may further enable high current densities during battery cycling, leading to both an ultrahigh power density and an excellent energy density.

In this regard, electrochemically active materials with strong affinity to Li⁺ ions but passivated HER activity of HER are of our highest interest. Particularly, polyimides (PIs) are a group of synthetic molecules with reversible redox capability, and have recently been reported as lithium- or sodium-ion-battery anode materials,^[12–17] in which the intrinsic insulating behavior of PIs is resolved by the combination with conductive carbon materials.^[12–15] Nonetheless, due to the lack of sufficient surface engineering for HER passivation and charge transport, the voltage output, and the power density of these electrodes are still far from optimum. We first carried out density functional theory (DFT) calculations to investigate the molecular structures of PIs, using two simple examples, poly(naphthalene four formyl ethylenediamine) (PNFE) and poly(benzene four formyl ethylenediamine) (PBFE). The most active sites for hydrogen atom adsorption in the PI structures are oxygen atoms, which possess the minimum value of energy barriers for binding an H atom (Table S1 in the Supporting Information). In an electrolyte without Li⁺ ions, the activation barrier of the simulated reaction pathway of H₂ formation is 2.11 eV for PNFE (Figure 1a) and 1.94 eV for PBFE (Figure S1 in the Supporting Information), indicating an intrinsic sluggish response to HER. This high activation energy for H atom adsorption is general for different PI structures (Table S1 in the Supporting Information). In addition, during the battery charging process in a Li⁺-containing electrolyte, half of the active sites (O atoms) for both Tafel (2H_{adsorption} → H₂) and Heyrovsky (H_{adsorption} + H₂O + e[−] → H₂ + OH[−]) are occupied by Li⁺ ions (Figure 1b), leading to a higher energy barrier and more sluggish kinetics for H₂ formation. Subsequently, a larger potential window and much higher energy densities are expected.

Thus, based on our hydrogen-evolution passivation strategy and the aforementioned theoretical analysis, we have reported a polyimide (i.e., PNFE) nanosheet array structure uniformly grown on freestanding carbon nanotube (CNT) networks, for its passivated HER activities and electrochemical energy-storage performance as ARLIB anodes (Figure 1c). PNFE was grown in situ on and was fully covered over the underlying freestanding CNT networks, which serve as current collectors with a negligible contribution to capacity and Coulombic efficiency (Figure S2 in the Supporting Information), and afford a substantially passivated HER activity as well as capability for Li⁺ storage. As a proof-of-concept, the PNFE nanosheets supported by freestanding CNT networks (designated as PNFE/CNT) display an extremely

Y. Wang, X. Cui, Dr. L. Zhang, Prof. G. Zheng
Laboratory of Advanced Materials
Department of Chemistry
Collaborative Innovation Center of Chemistry
for Energy Materials
Fudan University
Shanghai 200433, China
E-mail: gzheng@fudan.edu.cn

Y. Zhang, Prof. X. Gong
Department of Physics
Fudan University
Shanghai 200433, China
E-mail: xggong@fudan.edu.cn



DOI: 10.1002/adma.201602583

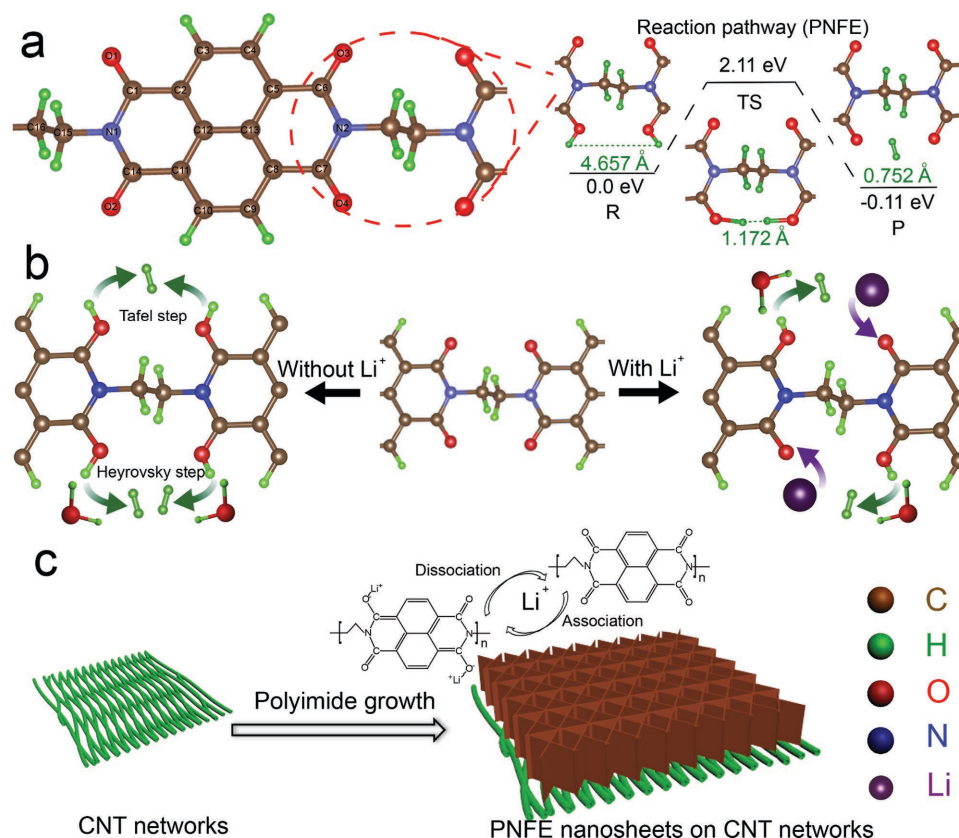


Figure 1. DFT calculation and schematic illustration of PNFE molecules for hydrogen evolution. a) Determination of the HER active sites and simulated Tafel-reaction pathway of HER on PNFE. b) Schematic illustration of further passivation of HER activity by reducing the number of active sites via Li⁺ association. The brown, green, red, blue, and purple spheres represent C, H, O, N, and Li atoms. c) Synthesis and lithium storage capability of PNFE nanosheets on CNT networks.

sluggish hydrogen-evolution process and large HER onset overpotential of 820 mV versus reversible hydrogen electrode (RHE), high reversible Li⁺-storage capacity and ultrafast rate capability (13.6 s per charge–discharge cycle) in aqueous solutions. Moreover, a full ARLIB cell with the PNFE/CNT anode and a LiMn₂O₄ cathode exhibit a wide discharge voltage range of 2.0 V, excellent energy density of $\approx 76.1 \text{ W h kg}^{-1}$ and power density of $\approx 12\,610 \text{ W kg}^{-1}$, based on the overall mass of both PNFE and LiMn₂O₄.

The freestanding CNT networks were composed of densely packed nanotubes, with lengths of over 10 μm and an average diameter of $\approx 20 \text{ nm}$ (Figure S3 in the Supporting Information). After the in situ polymerization (Methods in the Supporting Information),^[13] PNFE was deposited onto the CNT networks in large areas with uniform coverage and an average loading mass of $\approx 0.5 \text{ mg cm}^{-2}$ (Figure S4a in the Supporting Information). Scanning electron microscopy (SEM) images show that the PNFE/CNT network surface is covered with a layer of nanosheets perpendicularly aligned to the underlying substrate, with an average layer thickness of $\approx 10 \text{ nm}$ (Figure 2a,b). Similar morphology is also observed in the PBFE nanosheets grown on CNT networks (Figure S4b and S5a,b in the Supporting Information). The chemical structures of the as-synthesized PNFE and PBFE nanosheets were confirmed by Fourier transform infrared (FTIR) spectroscopy. For PNFE (Figure 2c), the peaks

at 1700 and 1670 cm^{-1} are assigned to the asymmetric and symmetric stretching vibrations of imide C=O bonds ($\nu_{\text{C=O, as}}$ and $\nu_{\text{C=O, s}}$), respectively.^[16] The absorption bands at 1385 and 1350 cm^{-1} are attributed to the stretching vibration of imide C–N groups ($\nu_{\text{C–N}}$).^[17] The bands located at 767 and 711 cm^{-1} are ascribed to the deformation vibration of imide C=O bonds ($\delta_{\text{C=O}}$).^[12] For PBFE (Figure S5c in the Supporting Information), the $\nu_{\text{C=O, as}}$ and $\nu_{\text{C=O, s}}$ bands are located at 1775 and 1725 cm^{-1} , respectively.^[14] The peaks at 1393 and 725 cm^{-1} correspond to $\nu_{\text{C–N}}$ of imide C–N bond^[16] and $\delta_{\text{C=O}}$ of imide C=O bond,^[14] respectively. The Raman spectra of the PNFE/CNT and the pristine CNT networks were further measured (Figure 2d and Figure S5d in the Supporting Information). The two peaks at 1336 and 1581 cm^{-1} are ascribed to the D and G bands of CNTs, respectively.^[18] The value of R ($R = I_{\text{D}}/I_{\text{G}}$), corresponding to the degree of graphitization of carbon materials, increases from 0.127 for pristine CNTs to 0.158 for PNFE/CNT and 0.277 for PBFE/CNT networks, indicating the formation of chemical bonds between CNTs and PIs.^[19]

To illustrate the theoretical calculation predictions, cyclic voltammetry (CV) was first employed to study the electrochemical HER behaviors of both the PNFE/CNT and PBFE/CNT networks (Figure 2e,f and Figure S6 and S7 in the Supporting Information). The CV curve of the PNFE/CNT measured in 0.5 M Li₂SO₄ aqueous solution presents two pairs of main redox

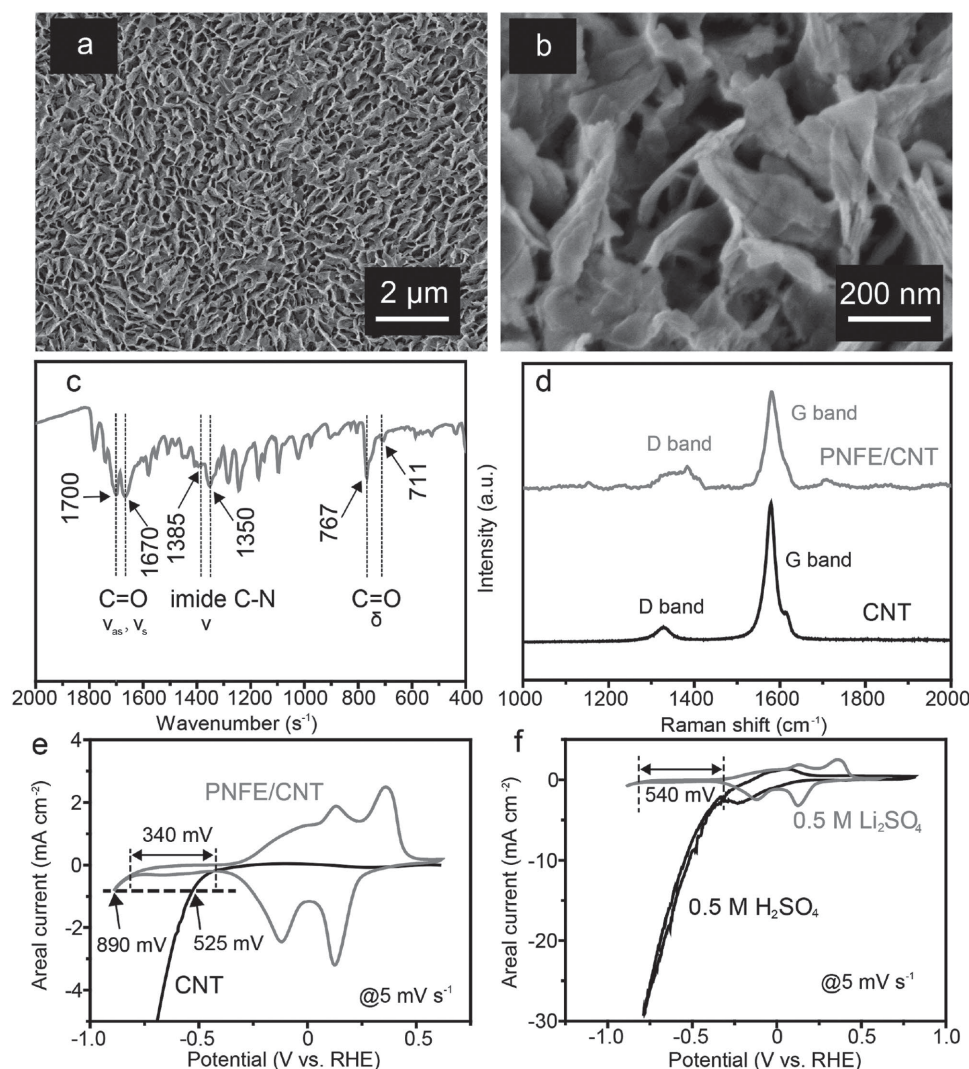


Figure 2. Morphology, structure, and electrochemical characterization of PNFE/CNT networks. a,b) SEM images of PNFE nanosheets grown on CNT networks. c) FTIR spectrum of PNFE nanosheets. d) Raman spectra of PNFE/CNT networks and pristine CNT networks. e) CV curves of PNFE/CNT networks and pristine CNT networks in 0.5 M Li_2SO_4 electrolyte. f) CV curves of PNFE/CNT networks in 0.5 M Li_2SO_4 and 0.5 M H_2SO_4 aqueous solutions, respectively.

peaks (Figure 2e), which are attributed to the association and dissociation of two Li^+ ions with the imide $\text{C}=\text{O}$ groups,^[12,15] as well as two electron transfers for each formula unit, delivering half of the theoretical capacity of PNFE.^[12] The hydrogen evolution does not take place until the applied overpotential exceeds 820 mV (Figure 2e), which is ≈ 340 mV larger than that of the plain CNT electrode (≈ 480 mV). Furthermore, the CV curves of the PNFE/CNT networks in 0.5 M H_2SO_4 and 0.5 M Li_2SO_4 were separately measured at the sweep rates of 5 mV s^{-1} (Figure 2f), which show that the onset overpotentials for hydrogen evolution are 280 and 820 mV, respectively. This 540 mV increase of hydrogen-evolution onset potential is mainly ascribed to the association of Li^+ ions on the O atoms of PI molecules, as the predominate factor for HER onset overpotential is the number of active sites instead of the pH value.^[20] In addition, for pristine CNT and PNFE/CNT networks, the overpotentials for obtaining 0.8 mA cm^{-2} HER areal current density in

0.5 M Li_2SO_4 aqueous solution are 890 and 525 mV, respectively (Figure 2e), and the Tafel slopes are calculated as 214.3 and $148.5 \text{ mV dec}^{-1}$ (Figure S6 in the Supporting Information), indicating that the growth and conformal coverage of PNFE on CNT substrate surface can further increase the overpotential for hydrogen evolution. Similarly, with the same prediction, the HER onset overpotential of the PBFE/CNT networks is measured as 740 mV (Figure S7 in the Supporting Information). These overpotentials of the PI structures substantially exceed most of the other materials,^[21,22] even for the CNT substrates beneath (Table S2 in the Supporting Information), suggesting PIs possess substantial passivation for hydrogen evolution.

The electrochemical properties of PNFE/CNT networks as aqueous energy-storage anodes were then investigated. To verify the passivated HER and stabilization effect during battery cycling, the PNFE/CNT networks were first operated at a low current rate of 0.2 C in the voltage range of -0.7 to 0.6 V

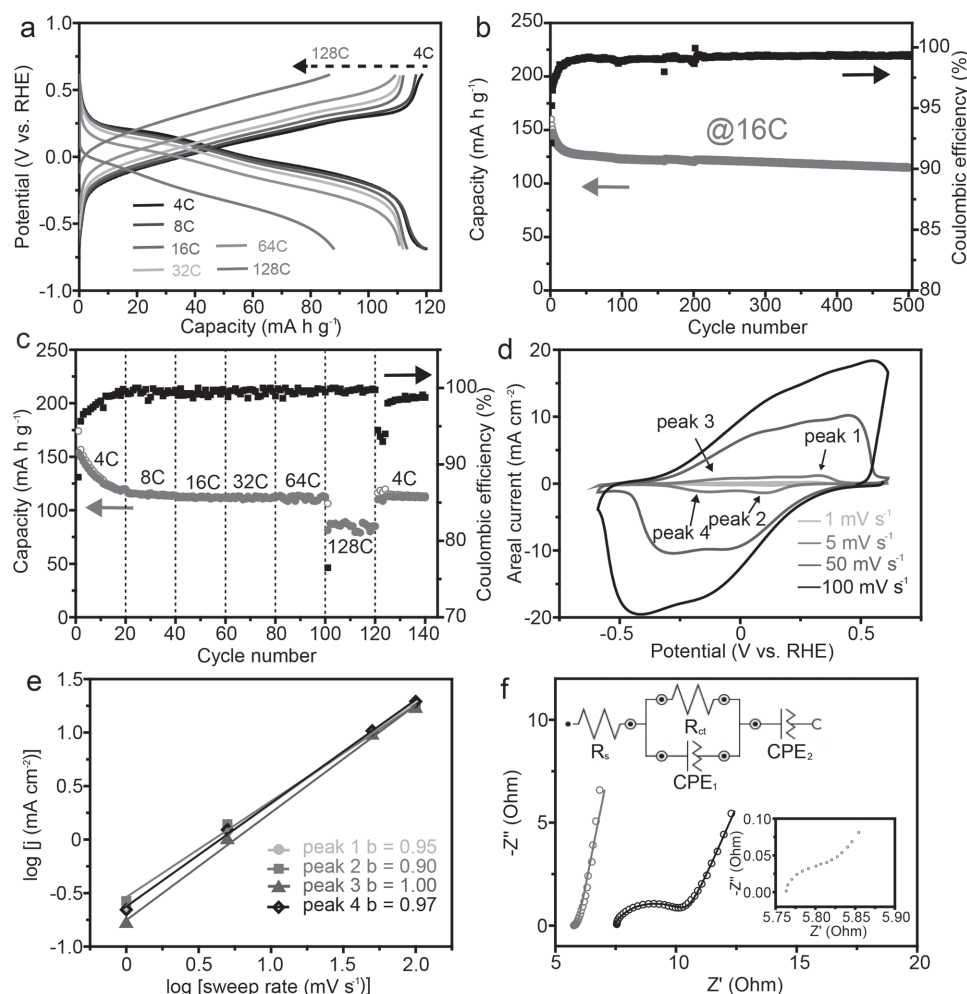


Figure 3. Electrochemical performances and kinetics analysis of PNFE/CNT networks as LIB anodes. a) Charge and discharge curves of PNFE/CNT networks at various current rates ranging from 4 to 128 C. b) Cycling stability of PNFE/CNT networks at a charge–discharge current rate of 16 C. c) Galvanostatic rate stability of PNFE/CNT networks at current rates ranging from 4 to 128 C. At a current rate of 128 C, the overall charge and discharge time is 13.6 s per cycle. d) CV profiles of PNFE/CNT networks at sweep rates of 1, 5, 50, and 100 mV s⁻¹. e) Determination of the *b* value for PNFE/CNT networks. f) EIS spectra of PNFE/CNT networks (left curve) and the electrode made by mechanical mixture of PNFE and conductive carbon black (right curve). Upper inset: corresponding equivalent circuit. Lower inset: enlarged EIS spectrum of the PNFE/CNT networks.

versus RHE for 100 cycles (Figure S8 in the Supporting Information). The charge–discharge and cycling profiles exhibit a high Coulombic efficiency of ≈99% with a reversible capacity of ≈130 mA h g⁻¹, indicating that HER is suppressed by the lithiated PNFE nanosheets. The fast charging–discharging capability and stability of the PNFE/CNT networks are demonstrated by increasing the current rate from 4 to 128 C (Figure 3a), corresponding to the fully operation time from ≈640 to ≈13.6 s per charge–discharge cycle. The PNFE/CNT networks exhibit an extraordinary cyclic stability at a high rate of 16 C, with 77.5% of capacity retention after 500 cycles (Figure 3b). In cycling performance test with different charge–discharge rates in the voltage range of -0.7 to 0.6 V versus RHE, the PNFE/CNT networks display an initial capacity of 153.7 mA h g⁻¹ at 4 C, which is well maintained with the fast increase of the current density (Figure 3c). Even at an ultrahigh charging–discharging current rate of 128 C (corresponding to an operation time of 13.6 s per charge–discharge cycle), the PNFE/CNT networks

still offers a discharge capacity of 86.2 mA h g⁻¹, which is 56.1% of the capacity at 4 C. The discharge capacity returns to 112.5 mA h g⁻¹ when the current rate is reset to 4 C, indicating its excellent reversibility. To the best of our knowledge, this charge–discharge time and related capacity substantially surpass most of the counterparts of the state-of-the-art anodes for aqueous energy-storage devices.^[4,5,23–25]

The ultrafast charge–discharge capability of the PNFE/CNT network anode was further investigated via kinetics analysis. For CV curves at various sweep rates from 1 to 100 mV s⁻¹, all the curves exhibit similar shapes with two broaden peaks in both cathodic and anodic processes (Figure 3d). According to the relationship between current and sweep rate:^[26]

$$j = av^b \quad (1)$$

the value of *b* can be calculated from the slope of log(*v*)–log(*j*) plots. Theoretically, if *b* = 0.5, the related electrochemical

process is totally diffusion-controlled, whereas $b = 1.0$ indicates a complete adsorption-controlled behaviour, corresponding to a capacitor-like process.^[27] In our experiments, the calculated b values for the four redox peaks are ranging from 0.9 to 1.0 (Figure 3e), suggesting an adsorption-predominant electrochemical property which endows PNFE the charge–discharge capability like supercapacitors.^[26–28] In addition, high electron conductivity is also critical to achieve this capacitor-like property. Thus, electrochemical impedance spectroscopy (EIS) analysis was performed to study the charge transport behaviors. For the PNFE/CNT network electrode (Figure 3f, left curve), the solution resistance (R_s) and charge-transfer resistance (R_{ct}) are calculated as 5.76 and 0.0981 Ω , respectively, much lower than those of the electrode made by a mechanical mixture of PNFE and conductive carbon black powder (Figure 3f, right curve, 7.43 and 3.01 ohm for R_s and R_{ct} , respectively). The PI molecular structure, combined with the capacitor-like kinetics, makes the PNFE/CNT networks as an ideal ARLIB anode material with ultrafast charging and discharging capabilities.

After the comprehensive study of the PNFE/CNT electrode in the three-electrode system, a PNFE//LiMn₂O₄ full-cell ARLIB was employed in 0.5 M Li₂SO₄ aqueous electrolyte as an example of energy-storage device, using the PNFE/CNT networks and LiMn₂O₄ as anode and cathode, respectively. The initial capacity of LiMn₂O₄ is ≈ 113 mA h g^{−1} at a current rate of 5 C_{LiMn₂O₄} (1 C_{LiMn₂O₄} = 140 mA g^{−1}, Figure S9a in the Supporting Information). The ARLIB was charged to an upper cutoff voltage of 2.4 V with a wide discharge voltage window of 2.0–0 V (Figure 4a and inset), with a charge and discharge current rate of 10 C_{PNFE} (based on the overall mass of PNFE and LiMn₂O₄), corresponding to each charge–discharge cycle within 5 min. As the low Coulombic efficiency and capacity of the LiMn₂O₄ cathode induced by the water oxidation restrict the electrochemical performance (Figure S10 in the Supporting Information) and do not reflect the quality of HER passivation,^[29] the low current rates (e.g., 0.2 C) was only applied for the anode materials. The initial discharge capacity of the PNFE//LiMn₂O₄ ARLIB is ≈ 68.8 mA h g^{−1}, based on the overall

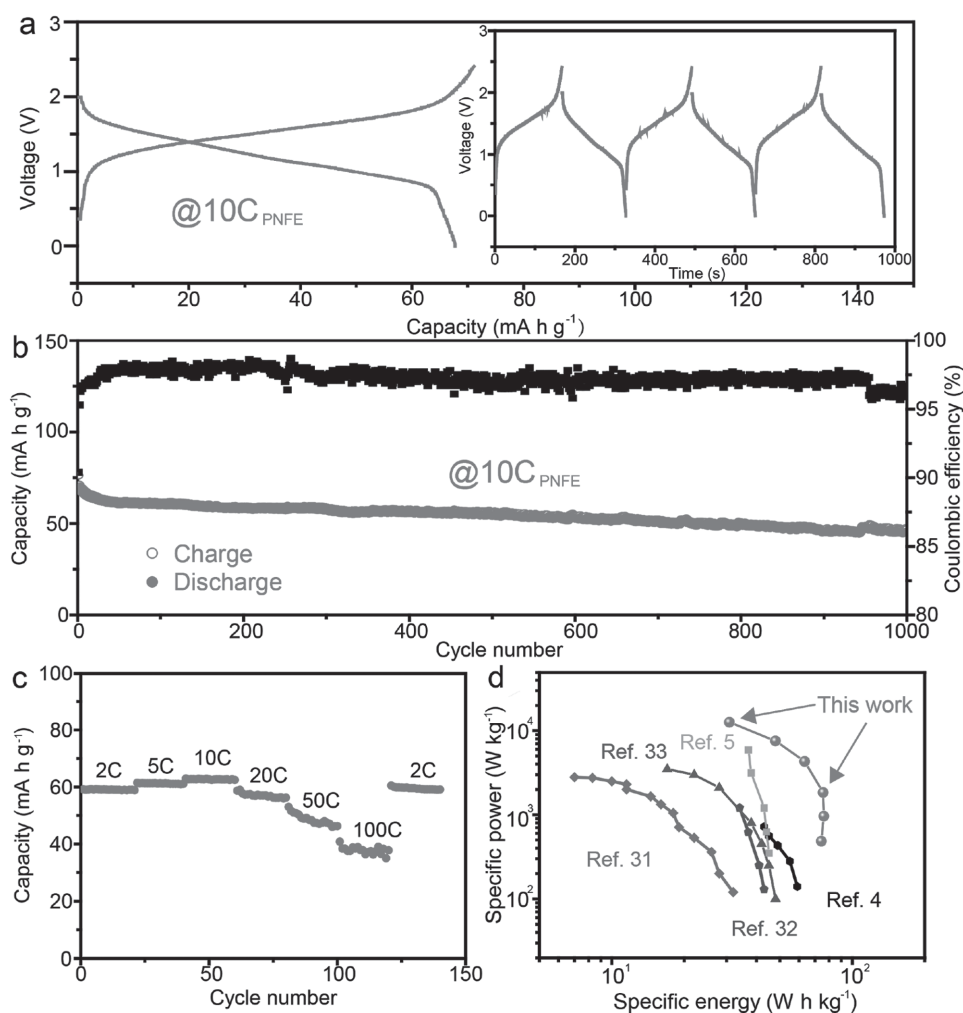


Figure 4. Performances of PNFE//LiMn₂O₄ ARLIBs. a) Galvanostatic charge and discharge profiles of a PNFE//LiMn₂O₄ ARLIB at a current rate of 10 C. Inset: charge and discharge curves displayed by voltage-versus-time plot. b) Long-term stability of a PNFE//LiMn₂O₄ ARLIB over 1000 cycles at a current rate of 10 C_{PNFE}. c) Rate discharge stability of a PNFE//LiMn₂O₄ ARLIB at current densities ranging from 2 to 100 C. d) Ragone plots of PNFE//LiMn₂O₄ ARLIBs. The values reported for other aqueous energy-storage devices are displayed for comparison.^[4,5,31–33]

mass of PNFE and LiMn_2O_4 . After 1000 cycles, the discharge capacity is retained at 45.1 mA h g^{-1} with a capacity retention of 65.5% (Figure 4b). The Coulombic efficiencies in majority of our 1000 cycles were ranging between 97% and 99%, except for the last 50 cycles (i.e., cycle 950–1000) the efficiency was $\approx 96\%$. The slight fading of Coulombic efficiency during the last 50 cycles is attributed to the electrochemical energy-storage process and capacity decay induced by long-term operation, similar to the recent literature,^[8] instead of the hydrogen production due to water splitting. The open circuit voltage (OCV) of a fully charged PNFE// LiMn_2O_4 can be retained at $\approx 1.52 \text{ V}$ after a standing time of 10 h (Figure S11 in the Supporting Information). A similar phenomenon was also reported previously in a polyimide// LiMn_2O_4 system with a much narrower voltage window,^[16] indicating that the OCV decay is ascribed to its capacitive mechanism of energy storage, instead of water splitting. The discharging rate measurement was then performed at the current rate ranging from 2 to 100 C (Figure 4c). The discharge capacity at 100 C (the corresponding discharge time is $\approx 8 \text{ s}$) is 37.6 mA h g^{-1} , which is 63.6% of the capacity at 2 C. Considering the poor Coulombic efficiency of the LiMn_2O_4 cathode at low current rates caused by oxygen evolution reaction (Figure S10 in the Supporting Information), the voltage window at low current densities (i.e., 2 and 5 C) was confined at 0–2.1 V (Figure 4c and Figure S9b in the Supporting Information), thus resulting in lower capacities and Coulombic efficiencies than those obtained at 10 C.

Finally, the specific power and energy of PNFE// LiMn_2O_4 ARLIBs were summarized and compared with representative records of aqueous lithium- and sodium-ion batteries reported previously (Figure 4d). A specific power of $\approx 12\,610 \text{ W kg}^{-1}$ is obtained at an energy density of $\approx 30.8 \text{ W h kg}^{-1}$ (upper arrow), and still remains at $\approx 1838 \text{ W kg}^{-1}$ when the specific energy increases to $\approx 76.1 \text{ W h kg}^{-1}$ (lower arrow). Compared with the state-of-the-art aqueous rechargeable alkali-ion batteries, such as $\text{VO}_2/\text{LiMn}_2\text{O}_4$,^[30] $\text{LiTi}_2(\text{PO}_4)_3/\text{LiMn}_2\text{O}_4$,^[4] $\text{MoO}_3@$ polypyrrole// LiMn_2O_4 ,^[5] $\text{LiTi}_2(\text{PO}_4)_3/\text{LiFePO}_4$,^[1] (polyaniline/ Fe_2O_3)// LiMn_2O_4 ,^[24] active carbon// LiMn_2O_4 ,^[31] $\text{NaTi}_2(\text{PO}_4)_3/\text{Na}_2\text{NiFe}(\text{CN})_6$,^[32] and $\text{NaTi}_2(\text{PO}_4)_3/\text{Na}_2\text{CuFe}(\text{CN})_6$,^[33] our PNFE// LiMn_2O_4 ARLIB holds a top-level performance in energy density, power density, and cycling life (Table S3 in the Supporting Information). This performance is also superior than that of polyaniline single-walled-CNT sponge-based supercapacitor,^[34] and close to that of ultrafast alkaline rechargeable Ni/Fe battery.^[35]

High theoretical specific power and safety are the two main factors making ARLIBs superior to conventional organic Li-ion batteries. Nonetheless, the low voltage window and limited specific energy induced by water splitting predominately restrict the battery practical performances. The approach of using highly concentrated organic Li^+ salt-based aqueous electrolytes can expand the voltage window, but it is hard to achieve high power density by this method.^[8] In our strategy, the increases of the voltage window and the energy density, while extremely high power density is maintained, are realized by passivation of the HER activity of active electrode materials. This passivation still exhibits a significant effect at a low current rate of 0.2 C, indicating the excellent chemical stability of our anodes. In addition, the conformal coating and passivation of

conductive substrates is also highly important for the inhibition of hydrogen evolution and improvement of the conductivity of active materials. Thus, ARLIBs with a wider voltage window, higher energy densities, outstanding specific power and excellent cycling performance are simultaneously realized.

As a new type of anode for aqueous alkali-ion batteries, PIs have very recently attracted attention.^[17,26] However, the influence of the PI structures to electrochemical hydrogen evolution, which is the critical bottleneck to ARLIBs, has still remained undiscovered, let alone the further substantial passivation via Li^+ association during charging. Although the redox potential range of PNFE/CNT network cannot fully cover its stable window before HER onset, this passivation still shows a new strategy to push the voltage window of ARLIBs. Their water splitting catalytic activity, redox potential, and Li^+ storage capability can be tuned via the design of the molecular structures.^[12] Thus, PIs represent a series of promising candidates for ARLIBs with much improved energy and power. Development of new organic materials with similar structures of PIs but lower content of hydrogen binding sites (e.g., only two O atoms per unit) may serve as an approach to better passivation of water reduction.

In summary, we have discovered the passivated HER activity of PNFE/CNT networks and further developed their high performance as anodes for ARLIBs. DFT calculations predict that PNFE possesses an intrinsic sluggish activity for HER catalysis due to their large activation barrier of 2.11 eV for HER, and the Li^+ association during charging can further reduce the active sites and increase the hydrogen-evolution overpotentials. With the rational design of electrode structure, capability of HER passivation and the capacitor-like Li^+ storage kinetics, the PNFE/CNT networks exhibit a large hydrogen-evolution onset overpotential of 820 mV versus RHE, outstanding reversible capacity of $153.7 \text{ mA h g}^{-1}$, and ultrafast rate capability as fast as 13.6 s per charge–discharge cycle. When combined with LiMn_2O_4 as cathode, the PNFE// LiMn_2O_4 full-cell ARLIB offers a wide voltage window ($>2.0 \text{ V}$), high specific capacity of 68.8 mA h g^{-1} at the charge and discharge current densities of 10 C, excellent energy density (76.1 W h kg^{-1}) and power density ($12\,610 \text{ W kg}^{-1}$), and extraordinary cycling stability (65.5% capacity retention after 1000 cycles when fast operated within 5 min), well exceeding most of aqueous energy-storage devices reported previously. Further design optimization of new molecular structures of PIs will lead to a promising avenue for new generation ARLIBs with much higher specific energy and power.

Supporting Information

Supporting Information is available from the Wiley Online Library or from the author.

Acknowledgements

Y.W., X.C., and Y.Z. contributed equally to this work. The authors thank the following funding agencies for supporting this work: the National Key Basic Research Program of China (2013CB934104), the Natural Science Foundation of China (21322311, 21473038), the Science and

Technology Commission of Shanghai Municipality (14JC1490500), the Program for Professor of Special Appointment (Eastern Scholar) at Shanghai Institutions of Higher Learning, and the Collaborative Innovation Center of Chemistry for Energy Materials (2011-iChem). The authors extend their sincere appreciation to the Deanship of Scientific Research at King Saud University for funding the Prolific Research group (PRG-1436-14).

Received: May 15, 2016

Published online:

-
- [1] J. Luo, W. Cui, P. He, Y. Xia, *Nat. Chem.* **2010**, *2*, 760.
[2] Y. Wang, J. Yi, Y. Xia, *Adv. Energy Mater.* **2012**, *2*, 830.
[3] M. Pasta, C. D. Wessells, N. Liu, J. Nelson, M. T. McDowell, R. A. Huggins, M. F. Toney, Y. Cui, *Nat. Commun.* **2014**, *5*, 3007.
[4] J. Y. Luo, Y. Y. Xia, *Adv. Funct. Mater.* **2007**, *17*, 3877.
[5] W. Tang, L. Liu, Y. Zhu, H. Sun, Y. Wu, K. Zhu, *Energy Environ. Sci.* **2012**, *5*, 6909.
[6] H. Kim, J. Hong, K. Park, H. Kim, S. Kim, K. Kang, *Chem. Rev.* **2014**, *114*, 11788.
[7] S. Liu, S. Ye, C. Li, G. Pan, X. Gao, *J. Electrochem. Soc.* **2011**, *158*, A1490.
[8] L. Suo, O. Borodin, T. Gao, M. Olguin, J. Ho, X. Fan, C. Luo, C. Wang, K. Xu, *Science* **2015**, *350*, 938.
[9] Y. Jiao, Y. Zheng, M. Jaroniec, S. Z. Qiao, *Chem. Soc. Rev.* **2015**, *44*, 2060.
[10] Q. Lu, Y. Yu, Q. Ma, B. Chen, H. Zhang, *Adv. Mater.* **2016**, *28*, 1917.
[11] X. Zhang, F. Meng, S. Mao, Q. Ding, M. J. Shearer, M. S. Faber, J. Chen, R. J. Hamers, S. Jin, *Energy Environ. Sci.* **2015**, *8*, 862.
[12] Z. Song, H. Zhan, Y. Zhou, *Angew. Chem. Int. Ed.* **2010**, *49*, 8444.
[13] H. Wu, S. A. Shevlin, Q. Meng, W. Guo, Y. Meng, K. Lu, Z. Wei, Z. Guo, *Adv. Mater.* **2014**, *26*, 3338.
[14] Y. Meng, H. Wu, Y. Zhang, Z. Wei, *J. Mater. Chem. A* **2014**, *2*, 10842.
[15] Z. Song, T. Xu, M. L. Gordin, Y. Jiang, I. Bae, Q. Xiao, H. Zhan, J. Liu, D. Wang, *Nano Lett.* **2012**, *12*, 2205.
[16] L. Chen, W. Li, Z. Guo, Y. Wang, C. Wang, Y. Che, Y. Xia, *J. Electrochem. Soc.* **2015**, *162*, A1972.
[17] W. Deng, Y. Shen, J. Qian, H. Yang, *Chem. Commun.* **2015**, *51*, 5097.
[18] J. Zhao, J. Chen, S. Xu, M. Shao, Q. Zhang, F. Wei, J. Ma, M. Wei, D. Evans, X. Duan, *Adv. Funct. Mater.* **2014**, *24*, 2938.
[19] R. Yuge, J. Miyawaki, T. Ichihashi, S. Kuroshima, T. Yoshitake, T. Ohkawa, Y. Aoki, S. Iijima, M. Yudasaka, *ACS Nano* **2010**, *4*, 7337.
[20] Z. Peng, D. Jia, A. Al-Enizi, A. Elzatahry, G. Zheng, *Adv. Energy Mater.* **2015**, *5*, 1402031.
[21] M. Gao, J. Liang, Y. Zheng, Y. Xu, J. Jiang, Q. Gao, J. Li, S. Yu, *Nat. Commun.* **2015**, *6*, 5982.
[22] D. Wang, M. Gong, H. Chou, C. Pan, H. Chen, Y. Wu, M. C. Lin, M. Guan, J. Yang, C. Chen, Y. Wang, B. Hwang, C. Chen, H. Dai, *J. Am. Chem. Soc.* **2015**, *137*, 1587.
[23] A. Caballero, J. Morales, O. Vargas, *J. Power Sources* **2010**, *195*, 4318.
[24] Y. Wang, Y. Wang, J. Tang, Y. Xia, G. Zheng, *J. Mater. Chem. A* **2014**, *2*, 20177.
[25] W. Tang, X. Gao, Y. Zhu, Y. Yue, Y. Shi, Y. Wu, K. Zhu, *J. Mater. Chem.* **2012**, *2*, 20143.
[26] X. Dong, L. Chen, J. Liu, S. Haller, Y. Wang, Y. Xia, *Sci. Adv.* **2016**, *2*, e1501038.
[27] C. Chen, Y. Wen, X. Hu, X. Ji, M. Yan, L. Mai, P. Hu, B. Shan, Y. Huang, *Nat. Commun.* **2015**, *6*, 6929.
[28] V. Augustyn, J. Come, M. Lowe, J. Kim, P. Taberna, S. Tolbert, H. Abruña, P. Simon, B. Dunn, *Nat. Mater.* **2013**, *12*, 518.
[29] N. Li, C. J. Patrissi, G. Che, C. R. Martin, *J. Electrochem. Soc.* **2000**, *147*, 2044.
[30] W. Li, J. Dahn, D. Wainwright, *Science* **1994**, *264*, 1115.
[31] Y. Wang, Y. Xia, *Electrochem. Commun.* **2005**, *7*, 1138.
[32] X. Wu, Y. Cao, X. Ai, J. Qian, H. Yang, *Electrochem. Commun.* **2013**, *31*, 145.
[33] X. Wu, M. Sun, Y. Shen, J. Qian, Y. Cao, X. Ai, H. Yang, *ChemSusChem* **2014**, *7*, 407.
[34] Z. Niu, W. Zhou, X. Chen, J. Chen, S. Xie, *Adv. Mater.* **2015**, *27*, 6002.
[35] H. Wang, Y. Liang, M. Gong, Y. Li, W. Chang, T. Mefford, J. Zhou, J. Wang, T. Regier, F. Wei, H. Dai, *Nat. Commun.* **2012**, *3*, 917.
-